Electronic Supplementary Material (ESI) for Environmental Science: Nano.

Supporting Information

A versatile test system to determine nanomaterial heteroagglomeration attachment efficiency

Helene Walch [a, 1], Nada Bašić [a], Antonia Praetorius [a, b], Frank von der Kammer [a, *], Thilo Hofmann [a, *]

[a.] *Department of Environmental Geosciences (EDGE), Centre for Microbiology and Environmental Systems Science (CeMESS), University of Vienna, Josef-Holaubek-Platz 2, A-1090 Vienna, Austria.*

[b.] *Department of Ecosystem & Landscape Dynamics, Institute for Biodiversity and Ecosystem Dynamics, University of Amsterdam, Science Park 904, 1098 XH Amsterdam, the Netherlands.*

* Corresponding authors.

E-mail addresses: h.walch@gmx.at, helene.walch@umweltbundesamt.at (H. Walch), nadaibasic@gmail.com (N. Bašić), a.praetorius@uva.nl (A. Praetorius), frank.kammer@univie.ac.at (F. von der Kammer), thilo.hofmann@univie.ac.at (T. Hofmann).

[1] *Present address: Studies & Consulting, Environment Agency Austria - Laboratories, Spittelauer Lände 5, 1090 Vienna, Austria.*

S1 – Natural river water characterization data

cations	[mg L^{-1}]	[mmol L^{-1}]	anions	[mg L^{-1}]	[mmol L^{-1}]
Ca	44.8	1.12	**SO_4^{2-}**	22.2	0.23
Mg	10.1	0.41	**Cl^-**	11.3	0.32
Na	7.22	0.31	**NO_3^-**	4.97	0.080
Si	2.08	0.074	**F^-**	0.089	4.7×10^{-3}
K	1.94	0.050	**PO_4^{3-}**	<LOD (0.50)	
Sr	0.174	2.0 × 10-3	**NO_2^-**	<LOD (0.31)	
Al	0.039	1.5 × 10-3	**Br^-**	<LOD (0.14)	
Ba	0.024	0.17×10^{-3}			
Cr	0.003	0.06×10^{-3}			
Mn	0.002	0.04×10^{-3}			
Fe	<0.014	$<0.26 \times 10^{-3}$			
Cu	<0.008	$<0.13 \times 10^{-3}$			
Cd	<0.001	$<0.01 \times 10^{-3}$			
Ni	<LOD (0.004)				
Pb	<LOD (0.006)				
Zn	<LOD (0.015)				

S2 – CeO_2 nanomaterial characterization

NM characterization included isoelectric point (IEP) determinations in different hydrochemistries (based on OECD TG 318), particle-number based size distribution by single particle (SP)-ICP-MS and scanning electron microscopy (SEM) imaging and sizing.

IEP determination

For IEP determinations, triplicate pH-titrations accompanied by zeta potential (ZP) measurements were conducted in different hydrochemical backgrounds (0-10 mmol L^{-1} electrolytes at a $CaCl_2$:$MgSO_4$ molar ratio of 4:2 and 0-10 mg L^{-1} Suwannee River NOM) based on the *alternative medium* in OECD TG 318 [1]. Zeta potentials were determined by electrophoretic light scattering (λ 633 nm, Zetasizer Nano ZS, Malvern) at a scattering angle of 17°. Each ZP measurement consisted of 20 runs of 3 s. Measurements were performed in folded capillary cells (DTS1070, Malvern) at CeO_2 concentrations of 100 mg L^{-1}. Titration curves and IEP results are shown below. Additional individual ZP measurements were conducted for CeO_2 in natural water and model water analog.

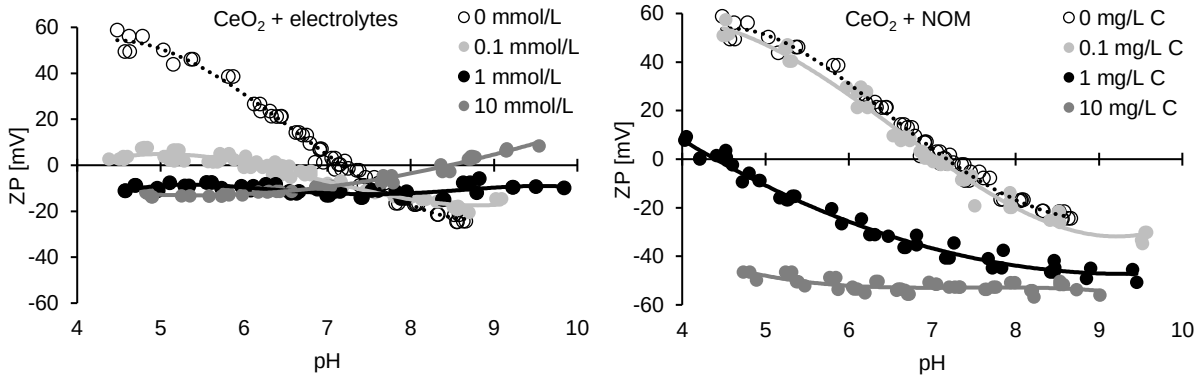

	Concentration of electrolytes [mmol L^{-1}] or SR-NOM [mg L^{-1}]			
	0	**0.1**	**1**	**10**
IEP CeO_2 + electrolytes	7.2 ± 0.1	6.1 ± 0.2	none	8.4 ± 0.2
IEP CeO_2 + SR-NOM	7.2 ± 0.1	7.0 ± 0.04	4.4 ± 0.2	none
	mV			
ZP CeO_2 in natural water	-14.5 ± 0.45			
ZP CeO_2 in model water	-16.1 ± 0.40			

Electrolytes as well as SR-NOM impacted the ZP of CeO_2. At acidic pH, the addition of electrolytes reduced the positive charge of CeO_2 and induced charge reversal at concentrations of 1 and 10 mmol L^{-1}. This is probably due to the adsorption of SO_4^{2-}, which is also indicated by the negative shift of the common intersection point of the titration curves at different electrolyte concentrations [2]. At alkaline pH, the opposite behavior was observed: increasing electrolyte concentrations reduced the negative charge of CeO_2 until, at 10 mmol L^{-1} and pH > 8.5, the surface turned slightly positive again. The same was observed for TiO_2 in the presence of $Ca(NO_3)_2$ [3] and can be explained by the adsorption of Ca^{2+} to negatively charged CeO_2. Since we used $CaSO_4$, SO_4^{2-} may also have acted as a bridge for Ca^{2+} adsorption. A similar mechanism has been described for phosphate and Ca^{2+} on ZrO_2 surfaces [4]. SR-NOM additions also added negative charge to the CeO_2 surface. At 10 mg L^{-1}, coating by SR-NOM established a highly

negative charge independent of pH. This is explained by the high density of negatively charged carboxyl groups (pK_a ~3) on SR-NOM [5,6].
The moderately negative ZP values in natural (nat.W) and model water (mod.W) suggest that NOM effects were dominated by electrolyte effects: the DOC concentration in nat.W and mod.W was ~2.5 mg L^{-1}, relevant electrolytes (Ca+Mg) ~1.5 mmol L^{-1}, and the pH 8.3 (see main text table 1). Without electrolytes present, that combination of SR-NOM and pH should induce a ZP of about -40 mV, as IEP titration curves suggest. However, with -16 mV, ZP is much less negative and rather in the range of titrations at 1 mmol L^{-1} electrolytes without SR-NOM (see above).

NM particle size distribution

CeO_2 particle size distribution was determined by SP-ICP-MS as described in the main text (section 2.2). On three different days, dilutions of the NM-stock (19.6 g/L) were prepared by four dilution steps (3 × 1:50 and 1 × 1:100) with acidified ultrapure water (pH ~5) to reach a concentration of 1.5 µg L^{-1}. From that suspension, triplicates (diluted 1:5) were prepared and measured by SP-ICP-MS. The size distributions (derived as described in S7) are shown below. Error bars represent standard deviations of triplicate measurements for each independent sample.

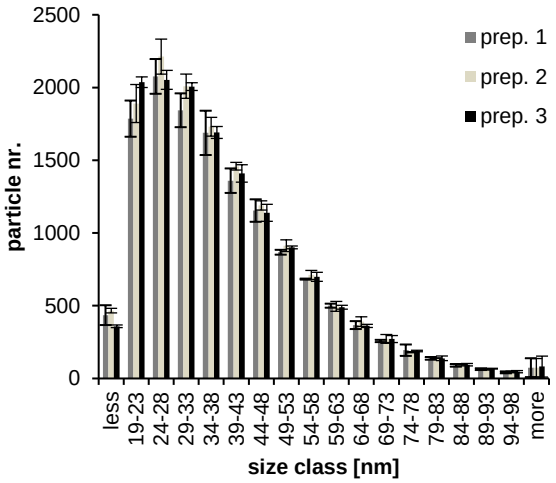

The mode particle size was ≥ 24 and < 28 nm, which is in accordance with the nominal size indicated (< 25 nm, BET). Size distributions cannot be fully explored by SP-ICP-MS since the smaller particles hit the particle size detection limit, which was determined to be 16.8 ± 0.5 nm (see S6).

SEM imaging

SEM imaging (10 kV, spot 3.5, WD 10 mm, ETD detector, Quanta 3D FEG, FEI) yielded shape and additional size information: 5 mL diluted stock suspension (concentration 1.1 mg L^{-1}) were deposited onto 0.02 µm filters (Ø 25 mm, Anodisc, Whatman) by vacuum filtration. The filters were oven-dried (55 °C) and carbon coated (EM SCD 500, Leica). As visible on the images below, shapes were rather irregular, from spherical to angular particles. The diameters of 65 particles were measured on SEM images, yielding an average diameter of 32 ± 15 nm and a median of 28 nm in accordance with the above.

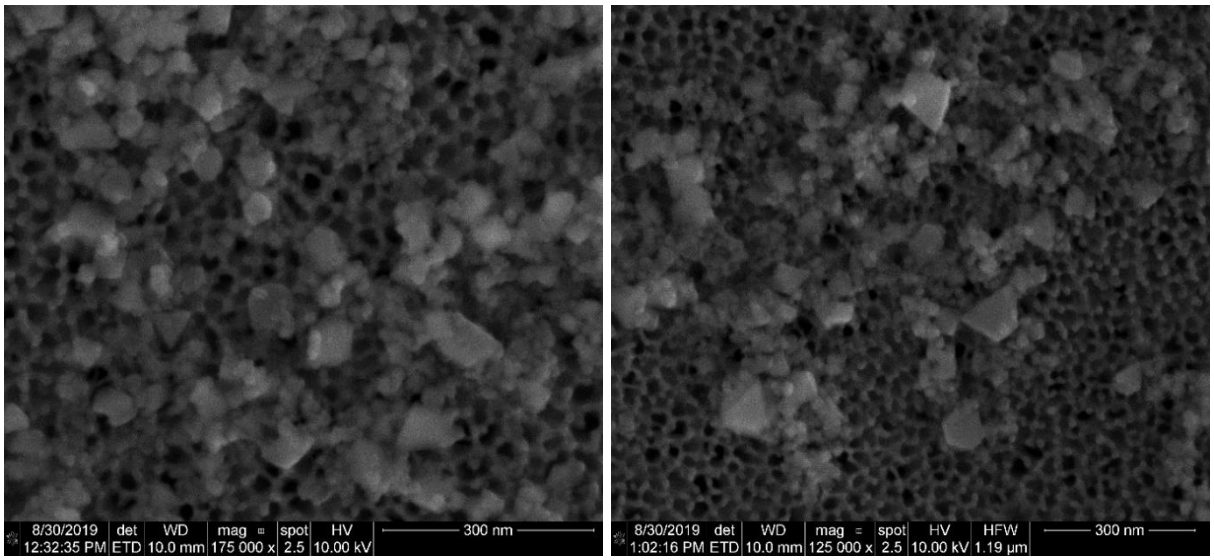

S3 – Stirred batch reactors

A batch reactor comprised a 1 L glass beaker (Duran) and a stirrer (RZR1, Heidolph) with a 7×7 cm 6-hole blade (Bochem). Batches were filled with 750 mL samples, and stirrers operated at 100 rpm, yielding an average shear rate (G) of ~97 s^{-1} (see S8). Dimensions (in mm) are indicated in the graph below.

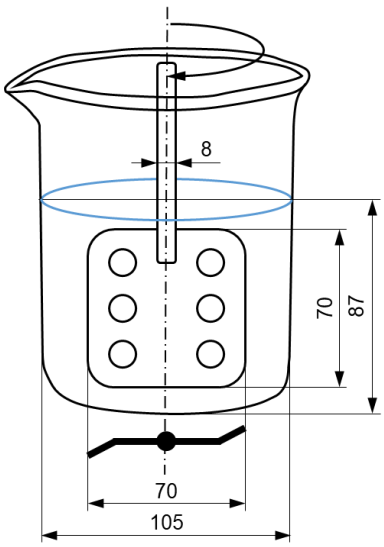

S4 – SPM suspension characterization

Volume- and number-based SPM size distributions

Volume-based SPM size distributions were measured by laser diffractometry (Mastersizer 2000, Malvern) as described before [7]. Briefly, angular light scattering patterns were recorded every 6-7 s (measurement duration 0.5 s), and volume-based size distributions were retrieved based on Mie theory, employing the general-purpose analysis mode and a refractive index of 1.544 (quartz). Size distributions were plotted from medians of 10 subsequent data records (covering ~60 s measurement time) taken when the size had stabilized (>1 h), just before the measurement was stopped and the suspension was transferred into experimental batches. Size class limits for size distributions ranged from 0.01-10,000 µm and increased by a factor of $10^{0.06}$ for each bin.

The volume-based size distributions were converted to number-based distributions by calculating the volume-concentration of SPM in the batch from the respective mass-concentration (45 or 20 mg L^{-1}), assuming an SPM floc density of 1.5 g cm^{-3}. The total SPM floc-volume was then distributed to the size bins according to the measured volume-based size distribution, and the SPM floc-numbers for each size class were approximated, assuming spherical floc shape and employing the lower size-class limit as floc diameter for each size bin. (The lower size limit was used as laser diffractometry is biased towards larger sizes.)

The figure below shows the number-based and volume-based size distributions of natural and model SPM (nat.SPM and mod.SPM) at 20 and 45 mg L^{-1} in natural (nat.W) and model water (mod.W) right before the experiments were started. Volume- and number-based size distributions deviated more strongly for nat.SPM than mod.SPM. Hydrochemistry slightly impacted the floc size: mod.W (dashed lines) slightly shifted size distributions towards smaller sizes; this was more pronounced for mod.SPM than nat.SPM and is probably related to different NOM-types (highly negatively charged SR-NOM in mod.W).

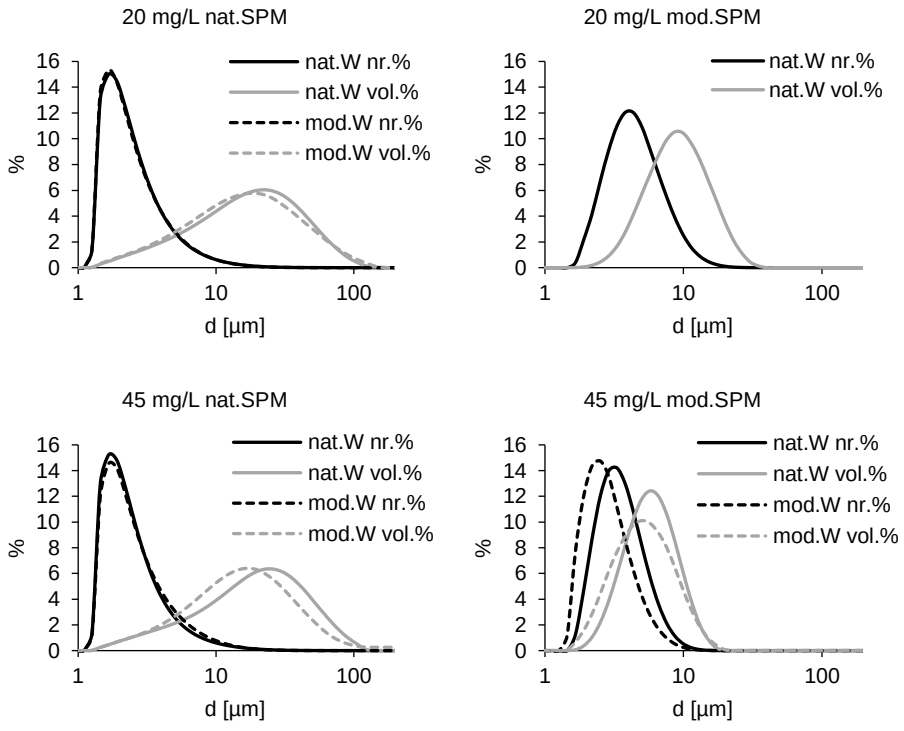

As shown below, the SPM concentration in the system had no effect on floc size of nat.SPM, but lower concentrations slightly increased the floc size of mod.SPM. The impact of concentration on mod.SPM size was reported before [7].

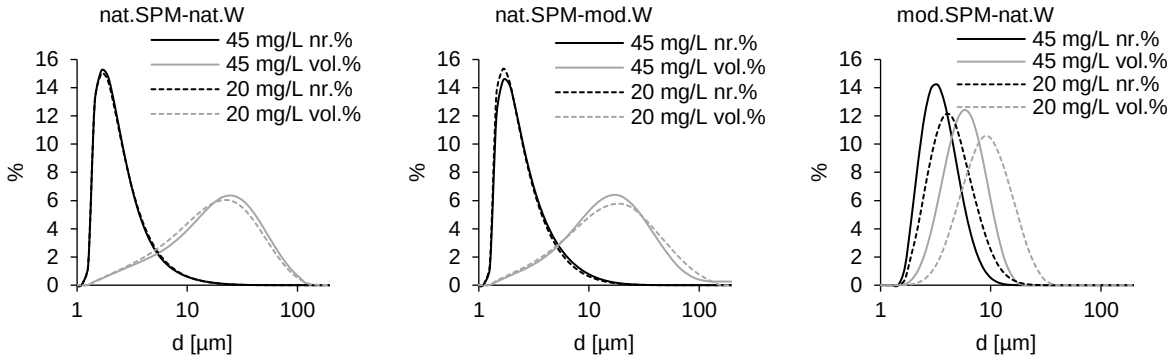

The figure below shows how raw water processing to natural floc stock affected size distributions after resuspension, with the left peaks depicting number-based size distributions and the right peaks showing volume-based distributions. Some of the very fine fraction was lost (probably during centrifugation), but else the size distributions were hardly changed.

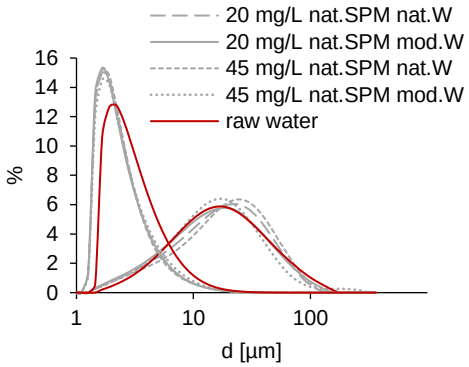

Fractal dimensions

The fractal dimension (D_f) describes the structural compactness of an agglomerate via the proportional relation ($m \propto r^{D_f}$) of mass (m) and agglomerate size (r) and takes values between 1 and 3. It can be determined from laser diffractometer data by generating a log-log plot of scattering intensities over scattering angles. The slope of the linear range of the fractal scattering regime in this plot corresponds to the fractal dimension. We determined fractal dimensions as described in Walch et al. [7], with one adjustment: The linear range of in the log-log plot was automatically determined as the best linear fit over 13 subsequent points on the curve (see the figure below). For that, coefficients of determination (R^2) of 7 subsequent points were calculated along the curve and moving averages over 7 subsequent R^2 values were calculated. The maximum of these values subsumed and thus identified the 13 points yielding the best linear fit.

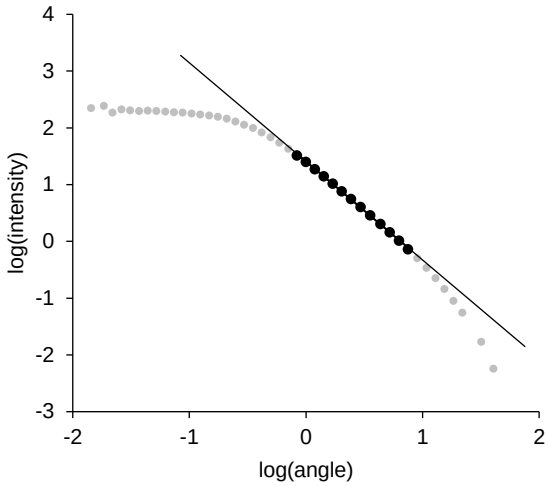

Fractal dimension values for raw water (raw.W), i.e., freshly sampled and sieved (125 µm) natural river water, and all SPM resuspensions at 20 and 45 mg L^{-1} are given in the figure below, and represent the fractal dimension measured over 20 minutes, when the floc size had stabilized in the stirred batch system. Fractal dimensions were similar between the two SPM concentrations, but mod.SPM were more compact (higher D_f) than natural flocs. Natural SPM in the raw river water sample was also more compact than in the resuspensions. This is likely an artefact of sample processing: especially sonication during resuspension may induce partial floc breakage and re-agglomeration yielding less compact structures [7].

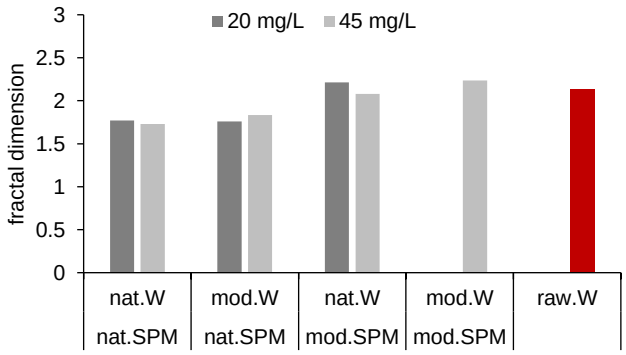

Zeta potential

Zeta potential (Zetasizer Nano ZS, Malvern) of SPM was measured in the raw water before SPM extraction and in 1 mL of SPM suspensions (45 mg L^{-1}) right before starting a heteroagglomeration experiment. The values are given in the figure below and indicate a more negative charge of mod.SPM, especially in nat.W.

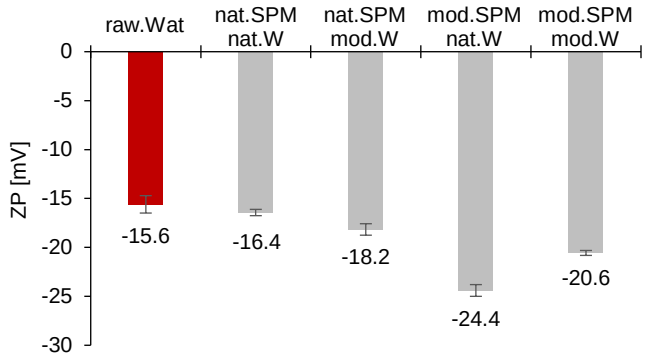

SEM images

For SEM imaging (see S2), 0.17 mL of 45 mg L^{-1} SPM suspensions, were diluted in 5 mL of the corresponding natural or model water and vacuum filtered (pore size 0.02 µm, diameter 25 mm, Anodisc, Whatman). Images of the raw water sample and the different resuspension combinations are shown below.

raw natural water sample

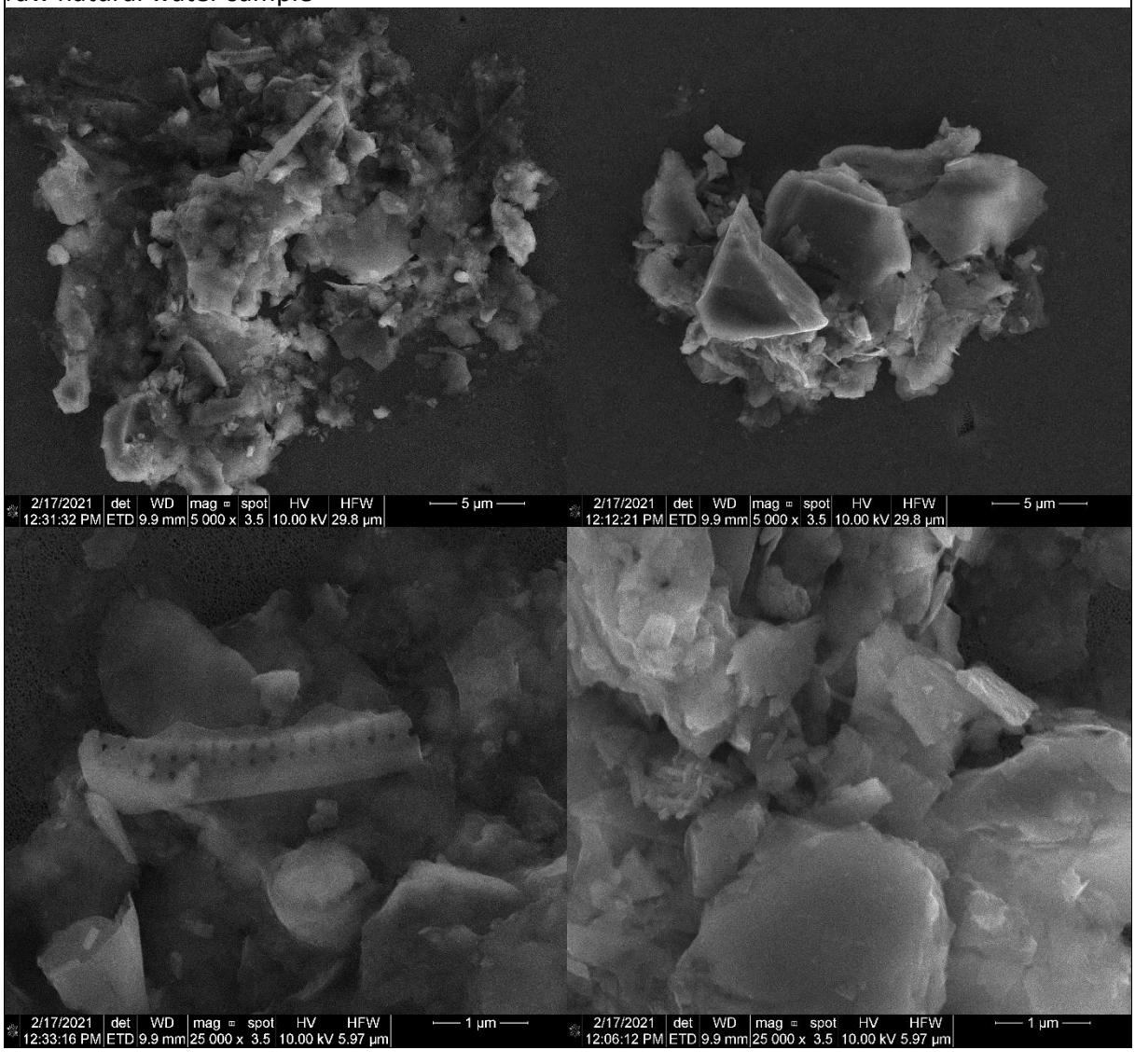

nat.SPM-nat.W

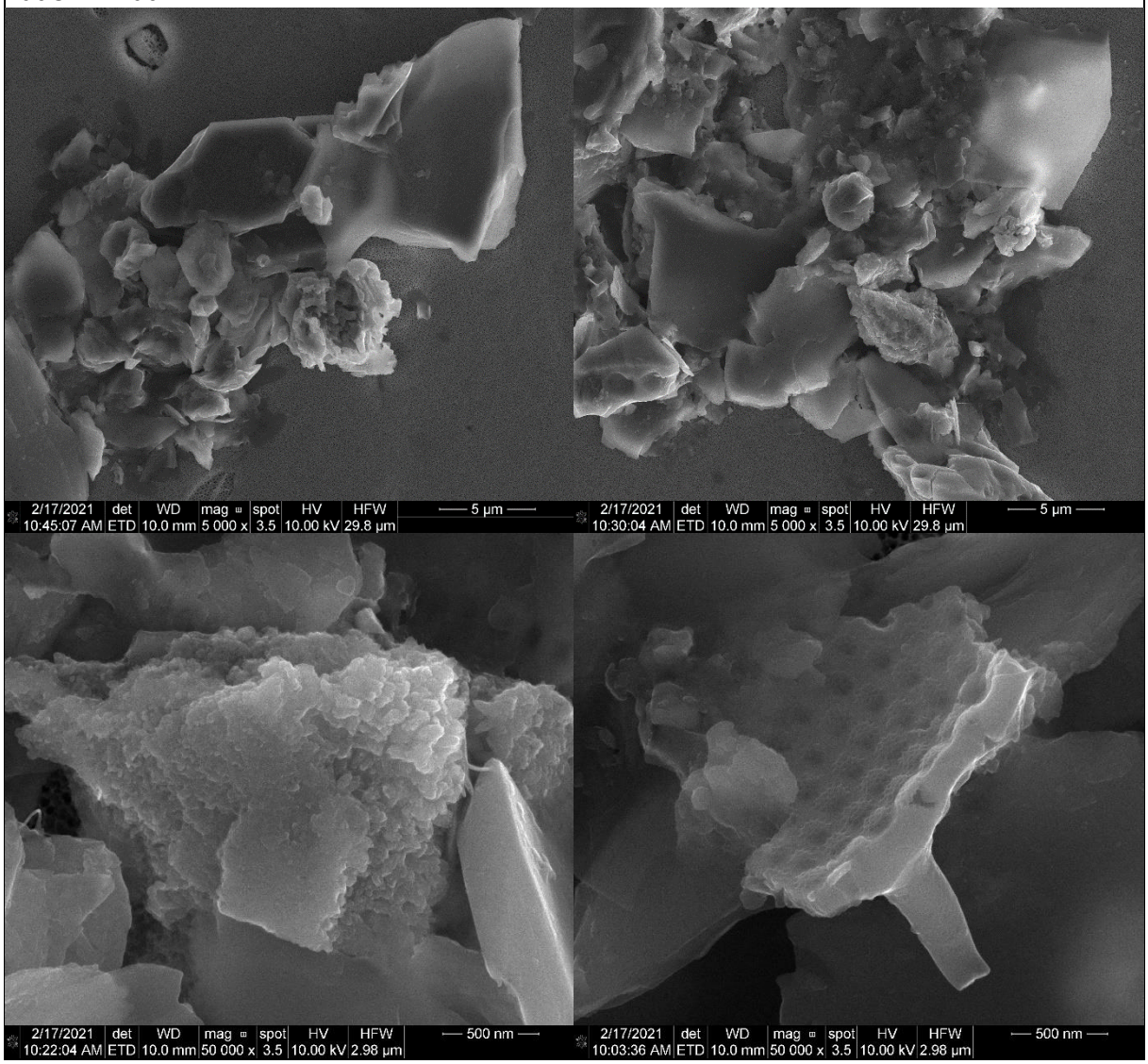
2/17/2021 10:45:07 AM
det ETD
WD 10.0 mm
mag 5 000 x
spot 3.5
HV 10.00 kV
HFW 29.8 µm
5 µm
2/17/2021 10:30:04 AM
det ETD
WD 10.0 mm
mag 5 000 x
spot 3.5
HV 10.00 kV
HFW 29.8 µm
5 µm
2/17/2021 10:22:04 AM
det ETD
WD 10.0 mm
mag 50 000 x
spot 3.5
HV 10.00 kV
HFW 2.98 µm
500 nm
2/17/2021 10:03:36 AM
det ETD
WD 10.0 mm
mag 50 000 x
spot 3.5
HV 10.00 kV
HFW 2.98 µm
500 nm

nat.SPM-mod.W

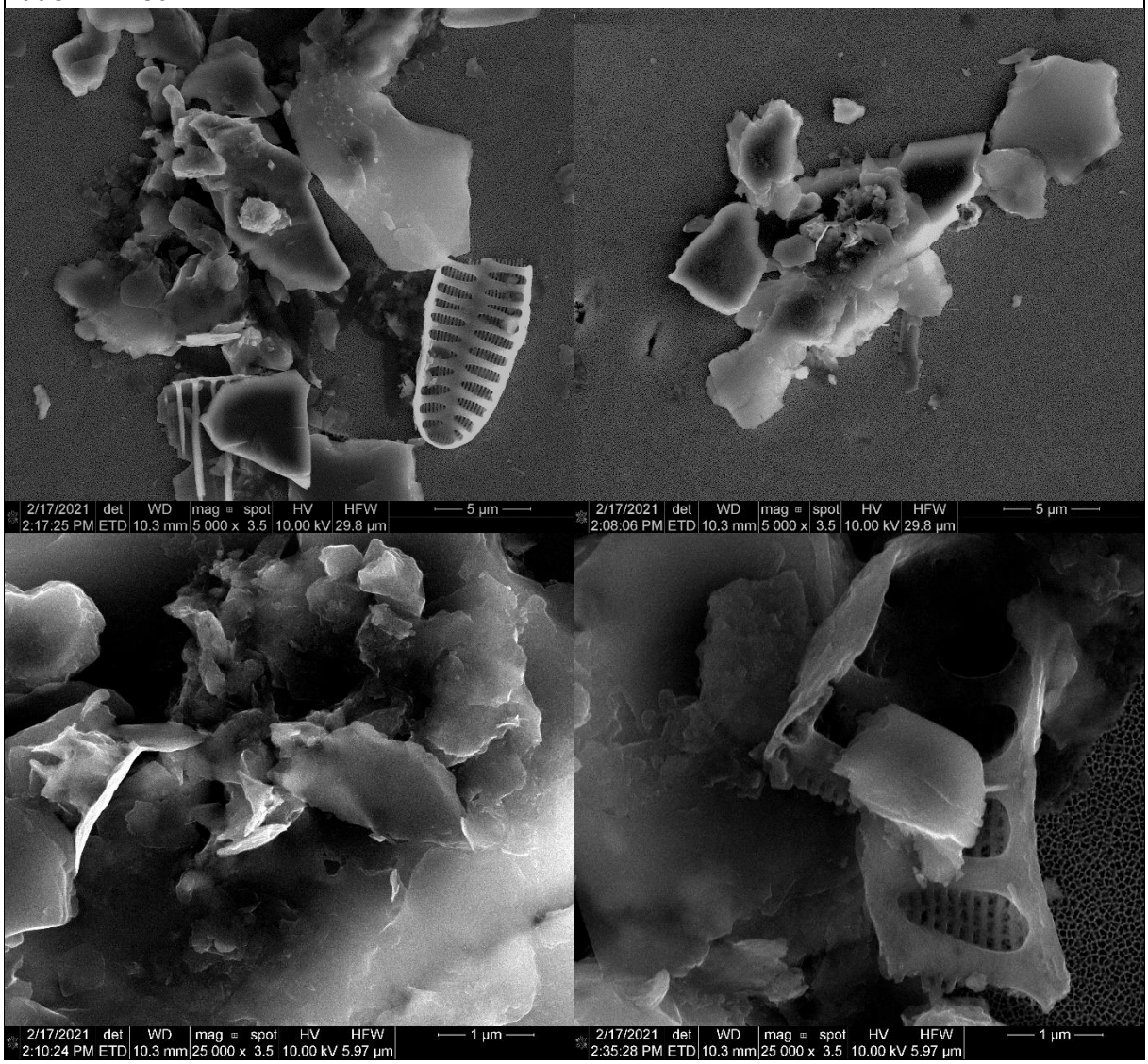
2/17/2021 det WD mag spot HV HFW 5 µm
2:17:25 PM ETD 10.3 mm 5 000 x 3.5 10.00 kV 29.8 µm
2/17/2021 det WD mag spot HV HFW 5 µm
2:08:06 PM ETD 10.3 mm 5 000 x 3.5 10.00 kV 29.8 µm
2/17/2021 det WD mag spot HV HFW 1 µm
2:10:24 PM ETD 10.3 mm 25 000 x 3.5 10.00 kV 5.97 µm
2/17/2021 det WD mag spot HV HFW 1 µm
2:35:28 PM ETD 10.3 mm 25 000 x 3.5 10.00 kV 5.97 µm

mod.SPM-mod.W

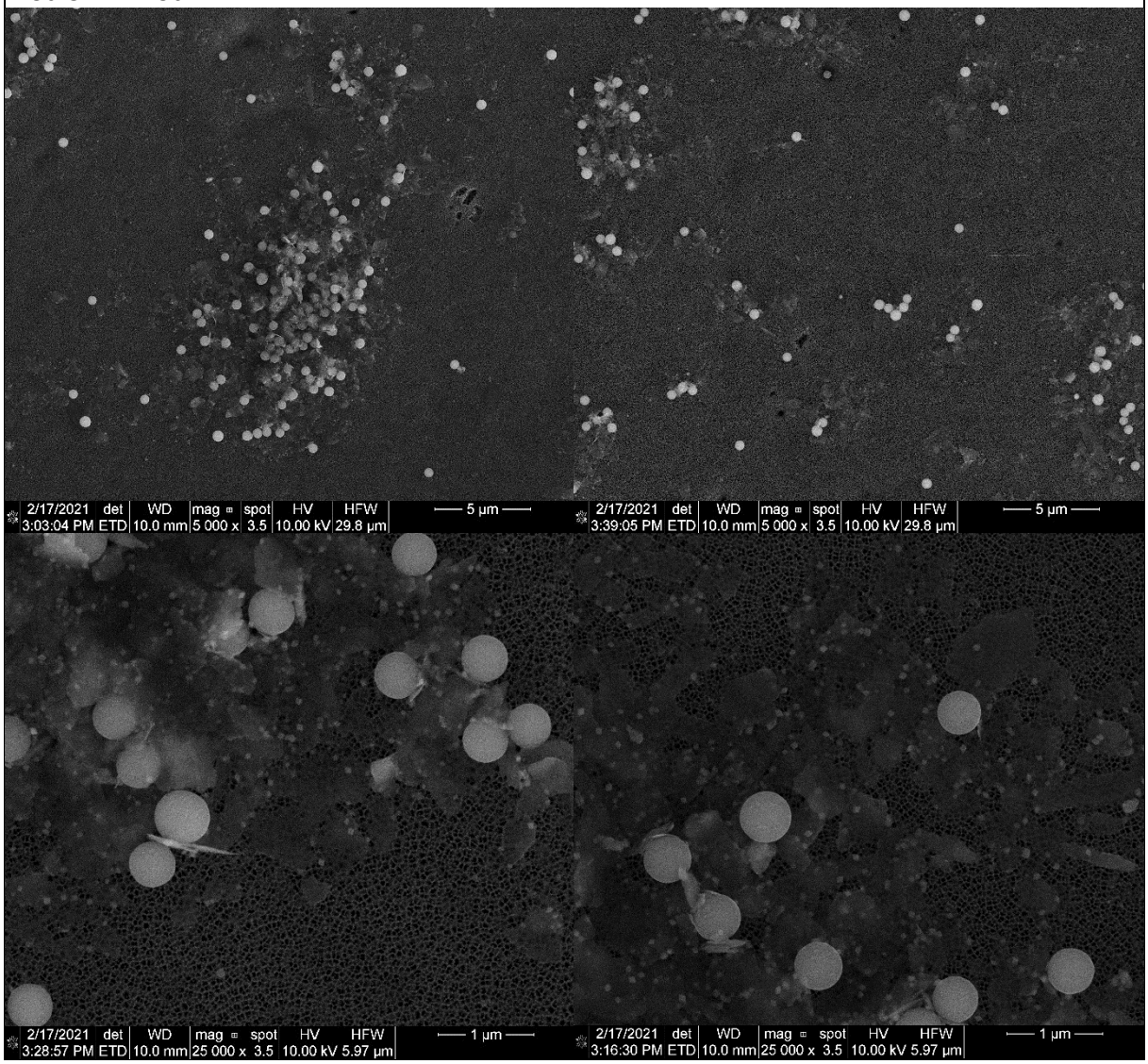
2/17/2021 det WD mag spot HV HFW
3:03:04 PM ETD 10.0 mm 5 000 x 3.5 10.00 kV 29.8 µm
5 µm
2/17/2021 det WD mag spot HV HFW
3:39:05 PM ETD 10.0 mm 5 000 x 3.5 10.00 kV 29.8 µm
5 µm
2/17/2021 det WD mag spot HV HFW
3:28:57 PM ETD 10.0 mm 25 000 x 3.5 10.00 kV 5.97 µm
1 µm
2/17/2021 det WD mag spot HV HFW
3:16:30 PM ETD 10.0 mm 25 000 x 3.5 10.00 kV 5.97 µm
1 µm

mod.SPM-nat.W

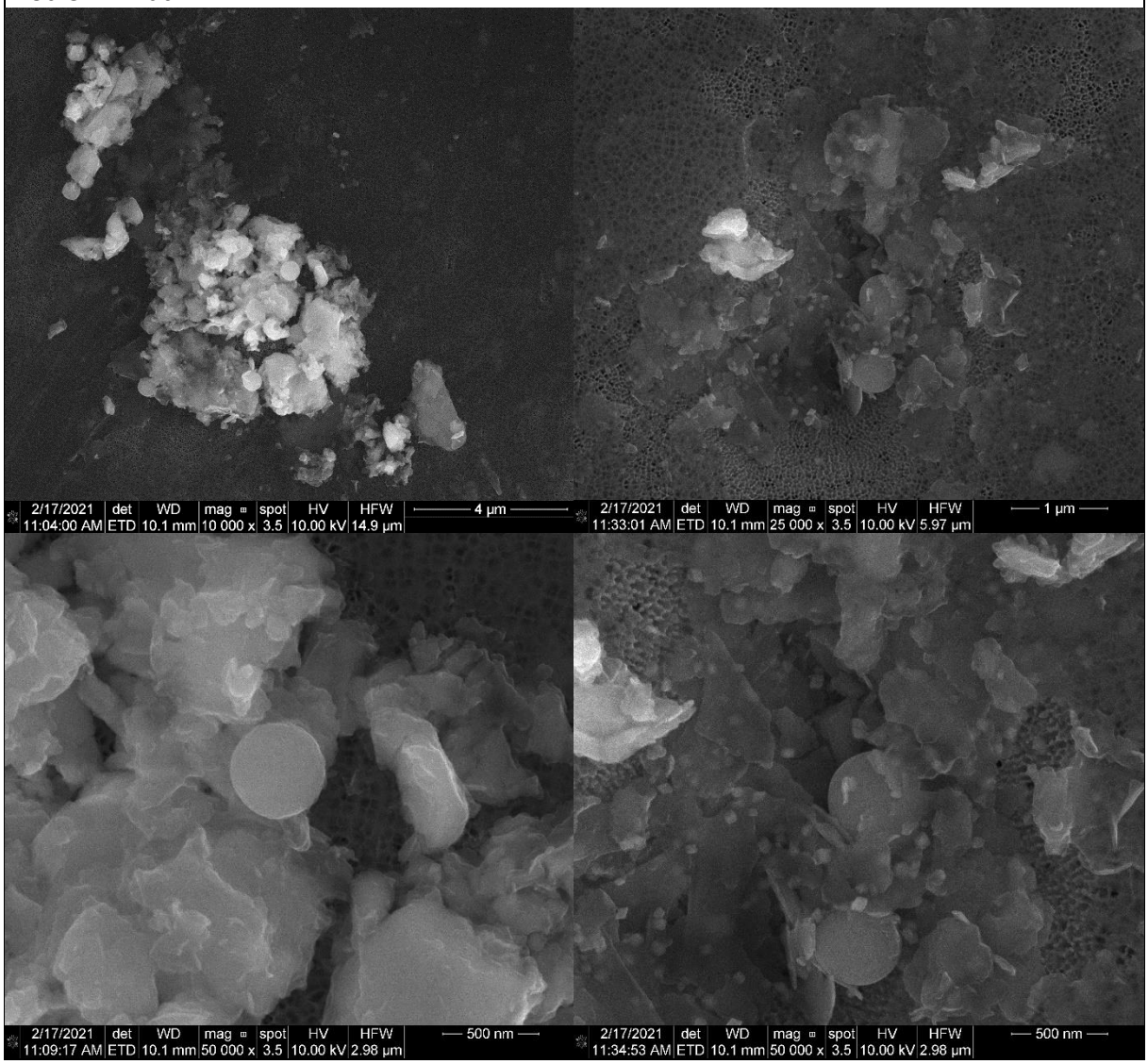
2/17/2021 11:04:00 AM
det ETD
WD 10.1 mm
mag 10 000 x
spot 3.5
HV 10.00 kV
HFW 14.9 µm
4 µm
2/17/2021 11:33:01 AM
det ETD
WD 10.1 mm
mag 25 000 x
spot 3.5
HV 10.00 kV
HFW 5.97 µm
1 µm
2/17/2021 11:09:17 AM
det ETD
WD 10.1 mm
mag 50 000 x
spot 3.5
HV 10.00 kV
HFW 2.98 µm
500 nm
2/17/2021 11:34:53 AM
det ETD
WD 10.1 mm
mag 50 000 x
spot 3.5
HV 10.00 kV
HFW 2.98 µm
500 nm

S5 – Separation of free and agglomerated NM by centrifugation

Approximation of screening effects during centrifugation

For heteroagglomeration experiments, samples were diluted (0.8 mL in 6 mL) before centrifugation to avoid NM losses due to screening effects, which SPM travelling towards the bottom may cause. The maximum potential screening effect was calculated for the employed 15 mL centrifuge tubes (inner diameter 13.6 mm) to demonstrate the effect of dilution prior to centrifugation. We assumed spherical shape of SPM and a density of 1.5 g cm^{-3} and calculated the number concentrations of SPM for the employed mass concentrations (i.e., 45 or 20 mg L^{-1} before dilution and 6 or 2.7 mg L^{-1} after dilution, respectively), using the average number-based mode diameter (d_{SPM}) of 4.5 µm to represent nat.SPM as well as mod.SPM (see S10). To calculate the impact of screening, a worst-case scenario was generated by considering the fraction of the tube cross-sectional area ($A\emptyset_{disc}$) which is passed by SPM cross-sectional area ($A\emptyset_{SPM}$) as fully screened (see graphs below). The sample volume (i.e., 4.5 mL) between the fill level (6 mL) and the 1.5 mL tube mark, which corresponded to a height h_{sV} of 31 mm, was divided into disc-shaped increments with a hight (h_{disc}) corresponding to d_{SPM}. Before centrifugation, each disc contains the same number of SPM (n_{SPM}), retrieved by dividing the total SPM number in the considered sample volume ($n_{SPM_{sV}}$) of 4.5 mL by the total number of discs (n_{discs}). During centrifugation, migration of SPM linearly increases the number of SPM that passed a disc with increasing depth. Consequently, the screened tube cross-sectional area increases from one disc (i) to the next (see graphs below).

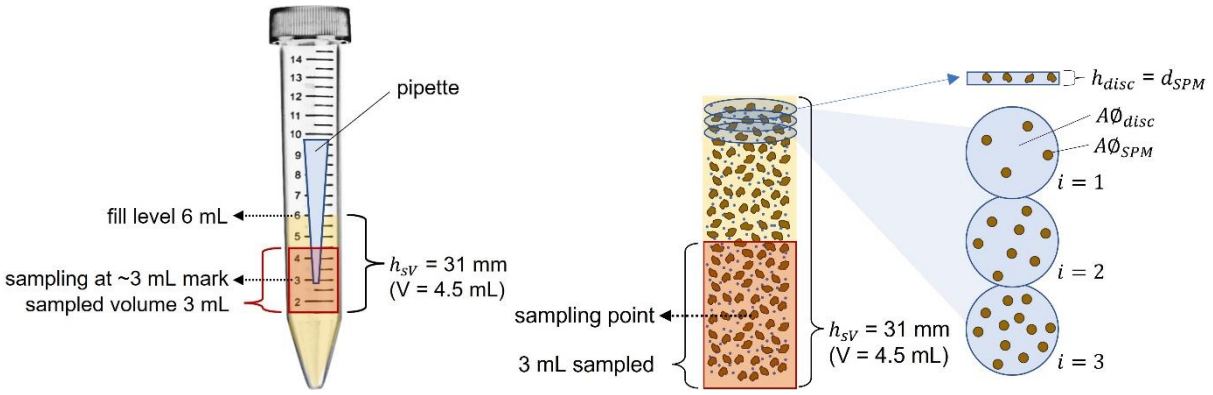

The screened cross-sectional area for each disc was translated to a screened volume by multiplication with the disc volume (V_{disc}), and the cumulative sample volume screened ($cumV_{scr}$) was calculated summing the screened volumes over all discs from $i = 1$ to $i = n_{discs}$, employing the equation below.

$$cumV_{scr} = \sum_{i=1}^{n_{discs}} i \, \frac{\frac{n_{SPM}}{disc} \, A\emptyset_{SPM}}{A\emptyset_{disc}} \times V_{disc}$$

$$n_{discs} = \frac{h_{sV}}{h_{disc}} \qquad h_{disc} = d_{SPM} \qquad \frac{n_{SPM}}{disc} = \frac{n_{SPM_{sV}}}{n_{discs}}$$

$cumV_{scr}$ cumulative screened sample volume [m^3]

n_{discs} total number of discs in the considered sample volume [-]

$n_{SPM}/disc$	number of SPM per disc [-]
$A\emptyset_{SPM}$	cross-sectional area of an SPM floc [m^2]
$A\emptyset_{disc}$	cross-sectional area of a disc (or the centrifuge tube) [m^2]
V_{disc}	disc volume [m^3]
h_{sV}	hight of the considered sample volume within the tube [m]
h_{disc}	disc height [m]
d_{SPM}	average number-based mode diameter of SPM (see S10) [m]
$n_{SPM_{sV}}$	total number of SPM in the considered sample volume [-]

The figure below shows the cumulative screened volume given as fraction of the total considered sample volume (4.5 mL between the 6 and 1.5 mL tube marks). Compared at the sampling point (slightly below the 3 mL tube mark), dilution reduced the potential impact of screening from about 7.5 and 3.5 % for 45 and 20 mg L^{-1} SPM concentrations, to <1 and <0.5 %, respectively. Since sampling with the pipette will draw sample volume from above and below the sampling point, as indicated by the shaded area in the graph, the screening effect without dilution may be even worse (up to 15.5 and 7 % for 45 and 20 mg L^{-1} SPM). In samples diluted prior to centrifugation screening still remains around 2 and 1 %.

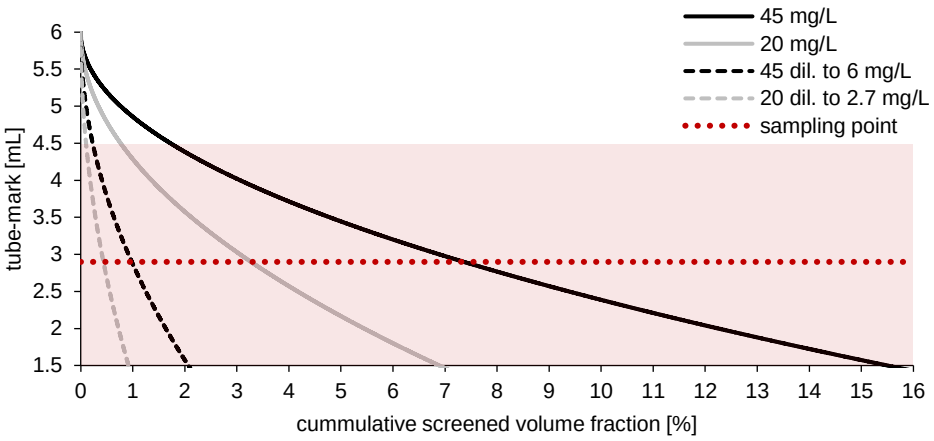

Selection of centrifugation parameters to separate heteroagglomerated from free NM

We employed centrifugation to separate heteroagglomerated from free NM particles. With a higher buoyant mass of SPM than NM, attached NM are removed with SPM during centrifugation, while free NM stay suspended.
Centrifugation time and speed were selected based on model calculations and pretests. To check the impact of centrifugation on CeO_2 NM, 15 mL of 50 µg L^{-1} NM suspension were filled into centrifuge tubes (15 mL, metal free, Carl Roth) and centrifuged for 0, 0.5, 2, 5, 15 and 35 min at 4500 rpm (CR 4.22, Jouan) in triplicates. With a pipette 1.5 mL were sampled at the 8 mL tube mark and diluted to 0.05 µg L^{-1} in acidified ultrapure water (pH ~5) for SP-ICP-MS measurements. Results, given in the figure below, showed no impact of centrifugation on CeO_2 particle concentrations.

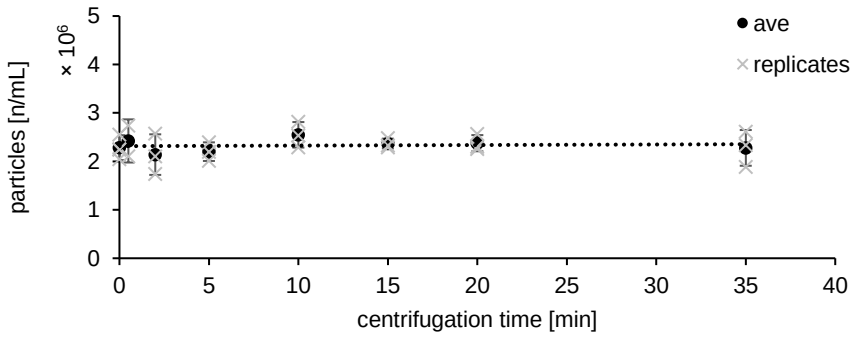

Model SPM suspensions (45 mg L^{-1}, pH 5, 0.1 mmol L^{-1} electrolyte background, i.e., 4:1 $CaCl_2$:$MgSO_4$) were also centrifuged at 4500 or 1700 rpm (CR 4.22, Jouan) for 5, 10, 15, 20, 35 min, and supernatants were analyzed on SP-ICP-MS for ^{56}Fe. Fe is a constituent of hematite (70 $\%_m$) and illite (5.5 $\%_m$), those components of model SPM that were small enough to remain suspended after centrifugation if not incorporated into SPM flocs. As a control, hematite and illite suspensions were prepared in acidified ultrapure water (pH~5) at their respective mass concentrations in the model SPM mix (i.e., 3.15 and 23.02 mg L^{-1}) and measured on SP-ICP-MS as well. The figure below shows that, compared to the non-centrifuged controls with only hematite or illite particles, the fraction of hematite or illite remaining suspended after the centrifugation of model SPM is insignificant, irrespective of centrifugation time or speed.

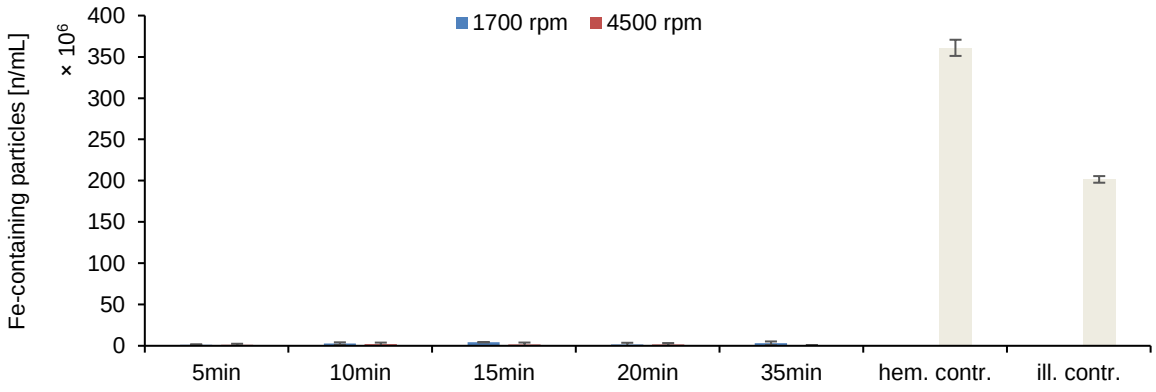

Based on the above, 6 min centrifugation time at 4500 rpm (4166 g) was found suitable to separate model SPM flocs from free NM particles with the table-top centrifuge (CR 4.22, Jouan).
To ensure natural SPM (and attached NM) removal by centrifugation with the table-top centrifuge during heteroagglomeration experiments, the extraction of SPM stock from raw water (see main text 2.1) with the Cryofuge (6000i, Heraeus) was performed at an equivalent centrifugal force. The equivalent centrifugation time for the Cryofuge operated at 4200 rpm (5897 g) was calculated to be 14 min. The clearance factors (k) for both centrifuges (A and B) were calculated, employing the equations below, and the equivalent centrifugation time (t) for centrifuge B (Cryofuge) was calculated by setting the sedimentation coefficients (S) equal, i.e., $S = \frac{k_A}{t_A} = \frac{k_B}{t_B}$.

$$k = \frac{\ln\left(\frac{r_{max}}{r_{min}}\right)}{\omega^2} \times \frac{10^{13}}{3600}$$

$$\omega = 2\pi \times \frac{rpm}{60}$$

$$t = \frac{k}{S}$$

k	clearance factor [s^2 rad^{-2}]
r_{max}	radius from rotor axis to sample tube bottom [m]
r_{min}	radius from rotor axis to sample fill-up point [m]
ω	angular velocity [rad s^{-1}]
t	centrifugation time [s]
S	sedimentation coefficient of particle [s rad^{-2}]

S6 – Setting background cut-offs for SP-ICP-MS

To select the signal background cut-off for SP-ICP-MS, frequency distributions of the signal intensities (counts) from blank samples were generated. The cut-off was set to ensure false-positive signals to be < 0.5 % for Ce in experimental matrix blanks (triplicates per batch), and < 0.05 % for Au in ultrapure water blanks. This was achieved by excluding all signals < 3 counts and resulted in 0.38 ± 0.06 % and 0.02 ± 0.02 % false positive signals for Ce in hetero- and homoagglomeration blanks and in 0.002 ± 0.001 % false positive signals for Au in ultrapure water. To further limit the chance that false positive signals yield false positive particle events, only three or more dwell-times in a row with signals ≥ 3 counts were considered a particle event. This yields a CeO_2 particle size detection limit of 16.8 ± 0.5 nm equivalent spherical diameter (d_P). The size detection limit was determined with the equation given in S7, employing a net particle intensity (NPI) determined as follows: The particle intensity of 9 counts (i.e., 3 dwell-times × 3 counts) was corrected for the average Ce counts/dwell-time measured in the respective experimental matrix blanks (triplicates per batch reactor) multiplied by the number of integrated dwell-times (i.e., 3).

S7 – Determining NM size distribution on SP-ICP-MS

An analyte-mass-based calibration is required to quantify the analyte mass related to a particle event. Since particles are discrete units, they do not convey a continuous mass flux into the plasma as dissolved analyte does. To account for that, the transport efficiency can be used [8]. It allows using a dissolved analyte calibration curve and correcting it for the particle mass-flux behavior. The transport efficiency is determined for particles of well-defined (narrow) size distributions, spherical shape, and known density, in our case 30 nm Au spheres (density 19,3 g/cm³, BBI Solutions). Assuming analyte NM particles of similar size behave the same way during sample introduction, the transport efficiency for Au particles can be employed to correct dissolved analyte (Ce) calibration curves for particle behavior.

Dissolved Ce and Au calibration curves included standards at concentration levels of 0.005, 0.025, 0.05, 0.25, 0.5, 5, 50 µg L^{-1}, prepared in 0.2 % HNO_3 and HCl, respectively. Au particle standards were diluted in ultrapure water to a nominal particle number concentration of ~1 × 10^6 mL^{-1} and analyzed for ^{197}Au in triplicates, employing the same instrument settings as for Ce SP-ICP-MS (see main text 2.2).

The signals (counts/dwell-time of 0.1 ms) related to a particle event were integrated by summing the counts per particle event (i.e., 3 or more dwell-times in a row with signals ≥ 3 counts, see S6) and noting the number of integrated dwell-times per particle. The median Au particle signal intensity was calculated and corrected for Au background by subtracting the average Au counts/dwell-time in ultrapure water blanks (n=9) multiplied by the median number of integrated dwell-times per particle; this yields the median net intensity per particle (NPI_{med}). The slope of the dissolved Au calibration curve ($slope_{dc}$) was used to determine the particle transport efficiency (TE) according to the equation below.

$$TE = \frac{m_P \; slope_{dc}}{flow \; t_d \; NPI_{med}}$$

TE	transport efficiency [-]
m_P	mass of 30 nm spherical Au particle [kg]
$slope_{dc}$	slope of Au dissolved calibration curve [counts m^3 kg^{-1}]
$flow$	sample introduction flow rate [m^3 s^{-1}]
t_d	dwell-time [s]
NPI_{med}	median net particle intensity [counts]

The transport efficiency is used to establish equivalent particle mass-flux calibration curves from the dissolved calibration curves employing the equation below.

$$PMF_{eq(x)} = c_{std(x)} \; flow \; t_d \; TE$$

$PMF_{eq(x)}$	equivalent particle mass-flux at calibration level x [kg $counts^{-1}$]
$c_{std(x)}$	analyte concentration calibration standard x [kg m^{-3}]

The slope of the equivalent particle calibration curve ($slope_{pc}$) is retrieved by plotting the average counts/dwell-time of dissolved calibration standards at all calibration levels (x) against the respective $PMF_{eq(x)}$. Equivalent spherical particle diameters (d_P) of NM particles can then be determined employing the equation below. The net signal intensity for each individual particle (NPI) was calculated analogously to NPI_{med} above, i.e., the particle signal intensity

was corrected for Ce background by subtracting the average Ce counts/dwell-time in experimental matrix blanks (triplicates per batch reactor) multiplied by the number of integrated dwell-times per particle. The ionization efficiency (IE) for Ce is 1, the density (ρ_P) of CeO_2 is 7,130 kg m^{-3}, and the mass fraction of analyte (f_m) in CeO_2 is 0.814.

$$d_P = \sqrt[3]{\frac{6}{\pi}\frac{NPI\ \ IE}{f_m\ \rho_P\ slope_{pc}}}$$

d_P	particle equivalent spherical diameter [m]
NPI	net particle intensity [counts]
IE	analyte ionization efficiency [-]
f_m	mass fraction of analyte [-]
ρ_P	density of particle [kg m^{-3}]
$slope_{pc}$	slope of particle calibration [counts kg^{-1}]

S8 – Deriving α_{het} from the pseudo-first-order heteroagglomeration rate constant (k^*_{het})

Deriving α_{het} from the pseudo-first-order heteroagglomeration rate constant (k^*_{het}) requires calculating the heteroagglomeration collision rate constant ($k_{coll,het}$) and the SPM number concentration (n_{SPM}).

$$k^*_{het} = -k_{coll,het}\, n_{SPM}\, \alpha_{het}$$

$k_{coll,het}$	heteroagglomeration collision rate constant [$m^3\ s^{-1}$]
α_{het}	heteroagglomeration attachment efficiency [-]
n_{SPM}	SPM number concentration [m^{-3}]

The heteroagglomeration collision rate constant is the sum of SPM-NM collisions through diffusion, advection, and differential sedimentation and was calculated as given below.

$$k_{coll,het} = \frac{2kT}{3\mu}\frac{(r_{SPM}+r_{NM})^2}{r_{SPM}r_{NM}} + \frac{4}{3}G(r_{SPM}+r_{NM})^3 + \pi(r_{SPM}+r_{NM})^2\left|\frac{2g}{9\mu}[(\rho_{SPM}-\rho_W){r_{SPM}}^2 - (\rho_{NM}-\rho_L){r_{NM}}^2]\right|$$

$k_{coll,het}$	heteroagglomeration collision rate constant [$m^3\ s^{-1}$]
k	Boltzmann's constant [$m^3\ kg\ s^{-3}\ K^{-1}$]
T	absolute temperature [K]
μ	dynamic viscosity of water (21°C) [$kg\ m^{-1}\ s^{-1}$]
r_{SPM}	radius of SPM floc [m]
r_{NM}	radius of nanomaterial [m]
G	shear rate [s^{-1}]
g	gravity acceleration [$m\ s^{-2}$]
ρ_{SPM}	density of SPM [$kg\ m^{-3}$]
ρ_{NM}	density of nanomaterial [$kg\ m^{-3}$]
ρ_W	density of water (21°C) [$kg\ m^{-3}$]

To approximate the shear rate (G), the following equation was used, and the power number (Ne) was derived employing the power characteristics established in Zlokarnik (2012, page 443) based on the similarity of stirrers (page 441, types B and C) and batch dimensions. The proportional relation of Ne and the Reynolds number (Re) for these stirrers is given below and holds for $10 \le Re \le 2 \times 10^4$.

$$G = \sqrt{\frac{Ne\ \rho_W\ rps^3\ d^5}{\mu\ V}} \qquad Ne = 30\ Re^{-\frac{1.17}{3}} \qquad Re = \frac{d^2\ rps\ \rho_W}{\mu}$$

Ne	power number [-]
d	stirrer blade diameter [m]
ρ_W	density of water (21°C) [$kg\ m^{-3}$]

rps stirring speed [rps]

μ dynamic viscosity of water (21°C) [kg m^{-1} s^{-1}]

V volume of liquid in batch [m^3]

Re Reynolds number [-]

We assumed a buoyant density of SPM of 1.5 g cm^{-3}. The densities of the mineral floc components illite, quartz, and hematite are 2.2, 2.0 and 5.3 kg m^{-3}, respectively. With a floc fractal dimension of around 2.2 (see S4), a floc density between 1.15-1.17 g cm^{-3} results if the following equation [10] is employed for each of the individual components (diameters used: illite 330 nm, quartz 500 nm, hematite 70 nm, SPM 4.5 µm). Since flocs consisted of a mix of these components and their different shapes (illite platelets, quartz spheres, hematite cubes), sizes, and concentrations probably allowed a more compact packing than spherical equal-size particles, we assumed a slightly higher SPM density of 1.5 gcm^{-3}.

$$\rho_{agg} = (\rho_P - \rho_W) \times (\frac{d_P}{d_{agg}})^{3-Df}$$

ρ_{agg} density of fractal agglomerate [kg m^{-3}]

ρ_P density of primary particle [kg m^{-3}]

ρ_W density of water (21°C) [kg m^{-3}]

d_P diameter primary particle [m]

d_{agg} diameter of fractal agglomerate [m]

Df fractal dimension of agglomerate [-]

The density of CeO_2 NM was 7.13 g cm^{-3}, according to the manufacturer.
For CeO_2 NM, a mode diameter of 25 nm was used (see S2). We tested employing the NM size distribution (see S2) instead, but due to the large size difference between NM and SPM, this had no impact on α_{het}.

SPM floc size and number were, for comparison, accounted for in two ways: **(1)** employing the **number-based mode diameter**, and **(2)** employing **number-based size distribution**.

Ad (1): The number-based SPM mode diameters were retrieved from number-based size distributions (see S4) as the lower size limit of the size class containing the maximum number of SPM flocs. Samples were measured right before the start of an experiment. The number-based mode diameters for all SPM-water combinations are displayed below (figure a) and were used to calculate SPM number concentrations from the SPM mass concentrations (45 or 20 mg L^{-1}), assuming spherical shape and a floc density of 1.5 g cm^{-3}. SPM number concentrations and diameters were then employed to calculate $k_{coll,het}$ and to derive α_{het} from k^*_{het}. For comparison, figure b gives the equivalent volume-based median diameters ($dV_{0.5}$) of raw and prepared samples. The floc size of the raw water sample right upon delivery to the lab (see main text 2.1.) is also included in the figures (in red).

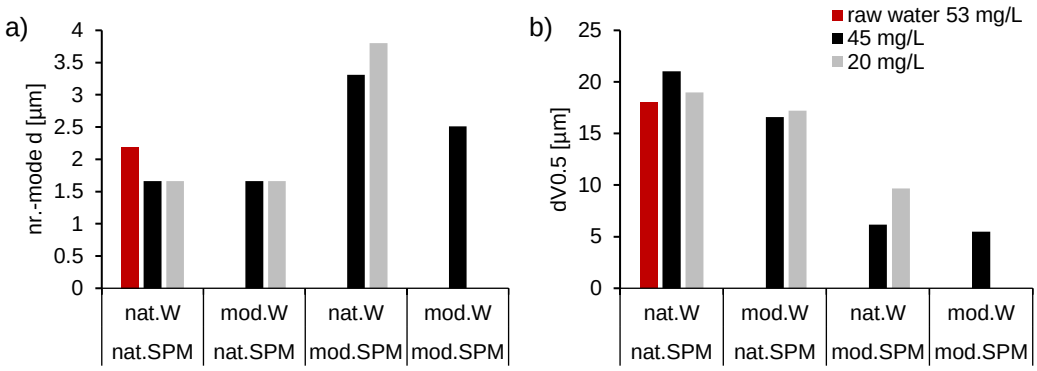

Ad (2): To account for the SPM floc size distribution, $k_{coll,het}$ was calculated for each SPM size class (i), employing the lower size class limit diameter, and multiplied with the respective SPM floc number concentration per size class (determined as described in S4). The resultant collisions per size class were summed, as given in the equation below, and the term (denoted $k^*_{coll,het}$) was employed to calculate α_{het} from k^*_{het}.

$$k^*_{coll,het}(size\ dis.) = k_{coll,het}(size\ dis.) \times n_{SPM}(size\ dis.) = \sum_{i=1}^{n} k_{coll,het(i)}\, n_{SPM(i)}$$

$k_{coll,het(i)}$ heteroagglomeration collision rate constant for SPM floc size class i [$m^3\ s^{-1}$]

$n_{SPM(i)}$ SPM number concentration in floc size class i [m^{-3}]

with $n_{SPM}(size\ dis.) = \sum_{i=1}^{n} n_{SPM\,(i)}$ and $k_{coll,het}(size\ dis.) = \frac{k^*_{coll,het}(size\ dis.)}{n_{SPM}(size\ dis.)}$

S9 – Sensitivity analysis of parameters in α_{het} determination

Sensitivity of α_{het} to parameter increase by 15%

The figure below shows the sensitivity of alpha determined for mod.SPM-mod.W experimental data to an increase of the respective parameters by 15% for the two cases of α_{het} calculation: (1) employing the number-based mode SPM diameter and (2) employing the SPM size distribution (see S8). The base scenario represented the following conditions: SPM concentration (cSPM) 45 mg L^{-1}, mod.SPM size (dSPM): either average number-based mode diameter 3.2 µm or average size distribution, SPM density (ρSPM) 1,500 kg m^{-3}, NM diameter (dNM) 25 nm, and stirrers operating at 100 rpm.
If the SPM size distribution is used, α_{het} is generally less sensitive to changes for all parameters (except stirring). In comparison to the number-mode SPM diameter, employing the size distribution increases the robustness of the α_{het} value due to an enhanced accuracy of SPM size, which strongly impacts the collision rate constant (see S8 and below.)

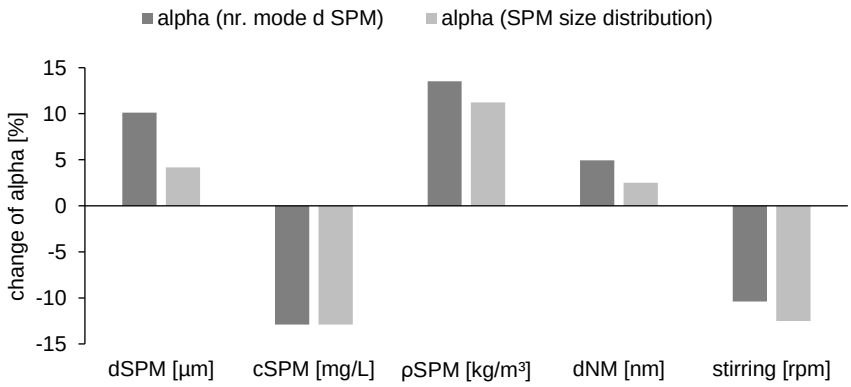

Impact of using number-based floc size distributions or mode diameters for α_{het} determination

Employing number-based size distributions instead of number-based mode diameters (see S8) for fixed SPM mass concentrations resulted in lower SPM number concentrations (figure a, below). The same is true for NM number concentrations, which in both cases exceed the SPM number concentrations by 1-3 orders of magnitude. In turn, the collision frequency (figure b) increases if size distributions are employed (due to the strong effect of larger SPM sizes on collisions). Overall, the product of the collision rate constant ($k_{coll,het}$) and (n_{SPM}), denoted $k^*_{het,coll}$ (see S8 and the equations below), decreases if size distributions are used. This explains higher α_{het} values for size distributions (figure 3, main text) since $k^*_{het,coll}$ is employed to derive α_{het} from the slope of the respective $\log(n_{NM})$-over-time plot. Generally, lower SPM numbers due to the presence of larger flocs yield fewer NM-SPM collisions.

$$k^*_{coll,het}(size\ dis.) = \sum_{i=1}^{n} k_{coll,het\,(i)} \times n_{SPM_{(i)}}$$

$$k^*_{coll,het}(nr.mode) = k_{coll,het} \times n_{SPM}(nr.mode)$$

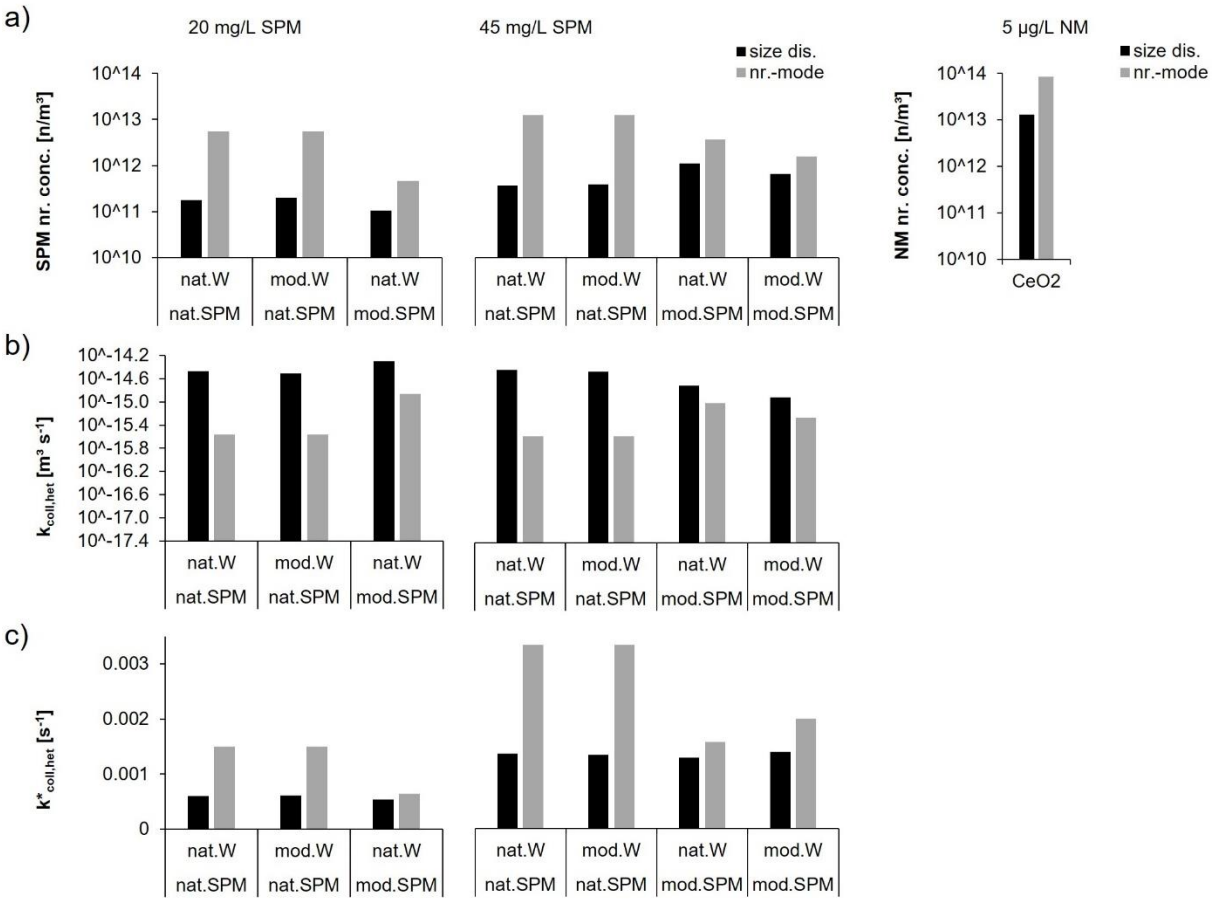
a)
20 mg/L SPM
45 mg/L SPM
5 µg/L NM
size dis.
nr.-mode
SPM nr. conc. [n/m³]
NM nr. conc. [n/m³]
10^14
10^13
10^12
10^11
10^10
CeO2
b)
10^-14.2
10^-14.6
10^-15.0
10^-15.4
10^-15.8
10^-16.2
10^-16.6
10^-17.0
10^-17.4
c)
0.003
0.002
0.001
0
nat.W
mod.W
nat.SPM
mod.SPM

S10– Homoagglomeration vs. heteroagglomeration

Ce mass-balance in homoagglomeration experiments

The Ce mass-balance for homoagglomeration experiments in mod.W and nat.W is given in the figures below. It shows the Ce-mass concentration in the top as well as in the bottom three mL of the samples after centrifugation at all sampling time points. In both hydrochemistries, the initial total mass concentration reflects the expected Ce mass concentration. In mod.W, the concentration was stable over time, with a slight but constant accumulation of Ce mass in the bottom 3 mL. This can be explained by a few larger and heavier NM particles migrating towards the bottom during centrifugation, which can significantly modify mass concentrations.
In nat.W, the total Ce mass decreased over time, indicating mass losses. While the top 3 mL exhibited constant Ce mass concentrations, losses became visible in the bottom fraction, indicating a preferential loss of larger/heavier NM. Since the bottom 3 mL were digested directly in the centrifugation tube, losses to the vessel or stirrer surfaces in the stirred-batch reactor are the only possible explanation.

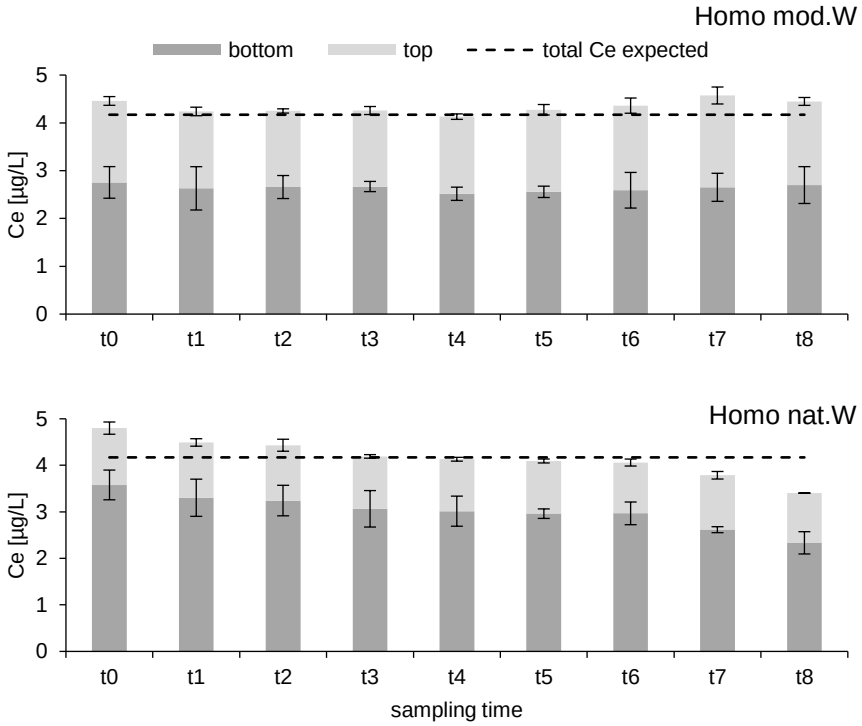

Smoluchowski-based model calculations

NM removal due to homoagglomeration and heteroagglomeration were modeled based on Smoluchowski's agglomeration theory (see equations 1 and 2 in the main text and S8) [11,12]. Involved parameters were set to represent experimental conditions, i.e., G~97 s^{-1} for stirring at 100 rpm, 45 mg L^{-1} SPM concentration, assumed SPM density of 1.5 g cm^{-3}, and 4.5 µm number-based mode SPM diameter. The latter results from varying the number-based mode diameters of model and natural SPM to find the values yielding the best fits with heteroagglomeration removal curves modeled employing the average number-based size distributions of nat.SPM and mod.SPM. The best-fit mode diameters were 4.2 and 4.9 µm for nat.SPM and mod.SPM, respectively. To represent both nat.SPM and mod.SPM size, the average (4.5 µm) was taken as number-based mode SPM diameter for all model calculations. Actually, deviations between

NM removal curves modeled for nat.SPM and mod.SPM were negligible, whether number-based mode diameters of 4.2, 4.5, or 4.9 µm were employed or the respective average number-based size distributions for nat.SPM or mod.SPM. The experimental setup is based on the assumption that small (nano-sized) SPM particles are incorporated into larger flocs and removed with them by centrifugation. This was ensured by extracting the SPM stocks by centrifugation/sedimentation and discarding the supernatants containing non-agglomerated small particles (see main text 2.1).
The initial NM number concentration ($n_{NM,t(0)}$) was calculated from the initial mass concentration (5 µg L^{-1}), assuming a spherical shape with a diameter of 25 nm and a density of 7.13 g cm^{-3} for CeO_2. The NM number concentration at time i was determined employing the equations below for homoagglomeration and heteroagglomeration to plot removal curves.

homoagglomeration: $n_{NM,t(i)} = n_{NM,t(i-1)} \times e^{k_{hom} n_{NM,t(i-1)} \mathrm{d}t}$

with $k_{hom} = -\alpha_{hom} \times k_{coll,hom}$

and $k_{coll,hom} = \frac{2kT}{3\mu} \frac{(2r_{NM})^2}{r_{NM}{}^2} + \frac{4}{3} G (2r_{NM})^3 + \pi (2r_{NM})^2$

heteroagglomeration: $n_{NM,t(i)} = n_{NM,t(i-1)} \times e^{k_{het} n_{SPM} \mathrm{d}t}$

with $k_{het} = -\alpha_{het} \times k_{coll,het}$

$n_{NM,t(i)}$ nanomaterial concentration at time i [n m^3]

k_{hom} homoagglomeration rate constant i [m^3 s^{-1}]

t time [s]

α_{hom} homoagglomeration attachment efficiency [-]

$k_{coll,hom}$ homoagglomeration collision rate constant i [m^3 s^{-1}]

The figure below shows that the removal of free NM by heteroagglomeration under the given conditions would always dominate that by homoagglomeration unless $\alpha_{hom} > \alpha_{het}$. Hetero- and homoagglomeration were calculated independently, i.e., the processes do not directly compete for NM removal.

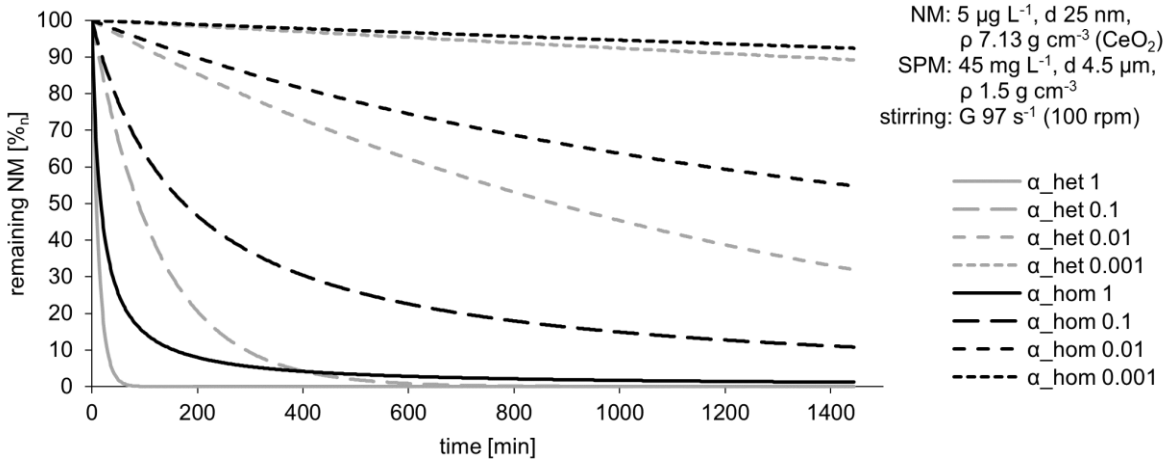

NM vs. SPM number concentrations

Environmentally relevant concentrations of NM are expected to be in the ng L^{-1} to few µg L^{-1} range [13,14], and SPM concentrations can range from <0.5 to >50,000 mg L^{-1} [15], but most frequently lie between a few to a few hundred mg L^{-1}. Considering the particle-mass to particle-number relation below, NM number concentrations can be higher than SPM number concentrations, especially at low SPM concentrations of few mg L^{-1} and/or at increased SPM floc size (e.g., at times of higher microbial activity, when flocculation is promoted [16]).

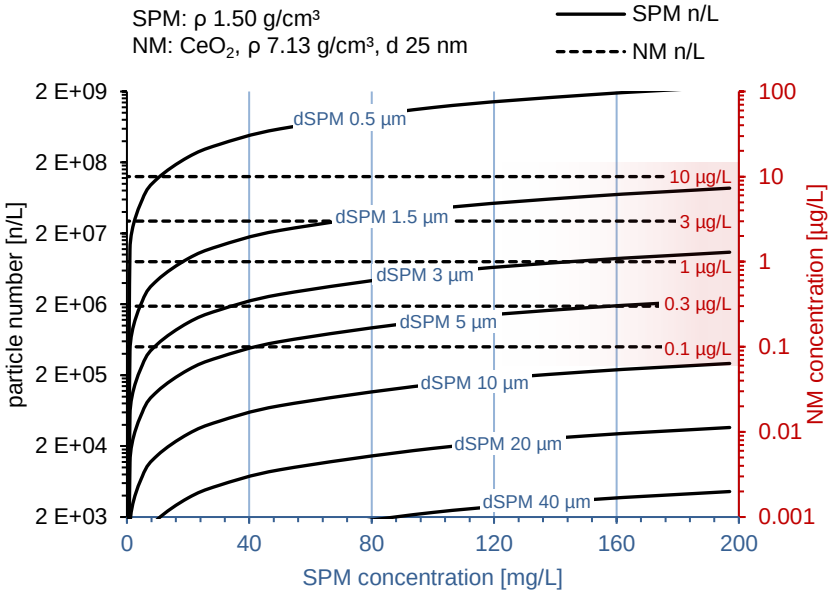

S11 – NM mass recovery and size in heteroagglomeration experiments

Ce mass recovery in digested samples (see main text 2.2) did not change over time in heteroagglomeration experiments, as shown in the graph below.

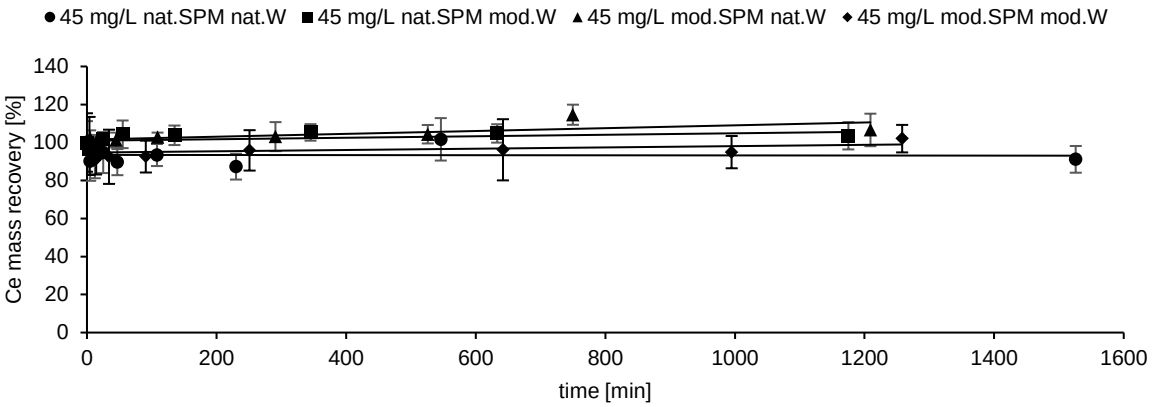

The CeO_2 median particle sizes (determined by SP-ICP-MS, see S7) did not change over time in heteroagglomeration experiments, confirming that no homoagglomeration co-occurred.

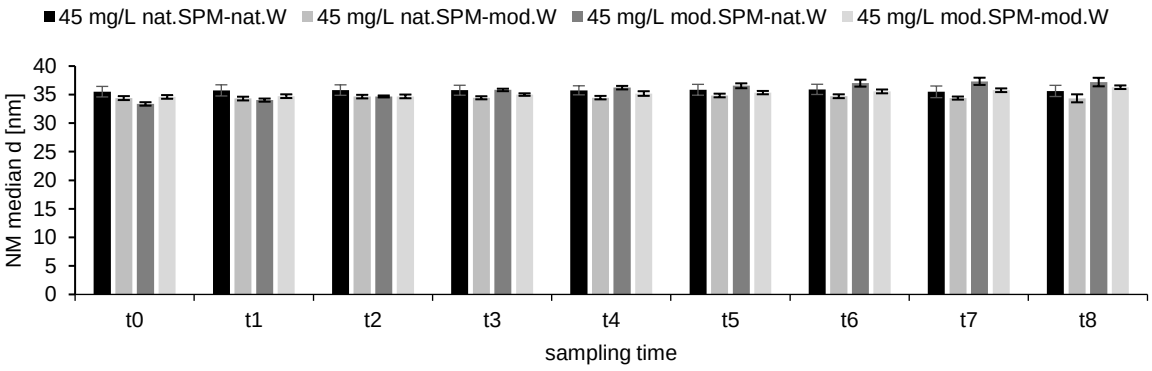

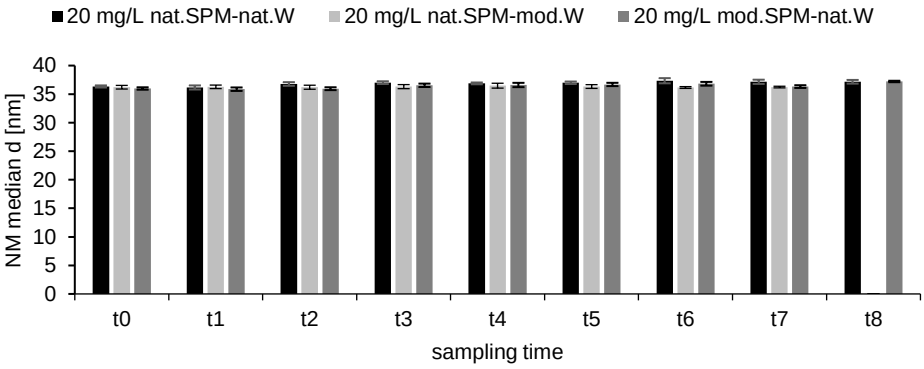

S12 – Heteroagglomeration half-lives

Since heteroagglomeration can be considered a pseudo-first-order reaction, the half-life ($t_{1/2}$) of non-agglomerated NM particles can be calculated employing the following equation. To calculate $k_{coll,het}$ and n_{SPM} (using the equations in S8), the involved parameters were set to represent experimental conditions, as described in S10 (Smoluchowski-based model calculations).

$$t_{1/2} = \frac{\ln(2)}{k_{het}^{*}} = \frac{\ln(2)}{\alpha_{het} \times k_{coll,het} \times n_{SPM}}$$

$t_{1/2}$ half-life of free, non-agglomerated NM particles [s]

REFERENCES

1 OECD, *Test No. 318: Dispersion Stability of Nanomaterials in Simulated Environmental Media*, OECD, Paris, 2017.

2 J. J. Gulicovski, I. Bračko and S. K. Milonjić, Morphology and the isoelectric point of nanosized aqueous ceria sols, *Mater. Chem. Phys.*, 2014, **148**, 868–873.

3 D. W. Fuerstenau, D. Manmohan and S. Raghavan, in *Adsorption From Aqueous Solutions*, Springer US, Boston, MA, 1981, vol. 13, pp. 93–117.

4 J. Lin, Y. Zhan, H. Wang, M. Chu, C. Wang, Y. He and X. Wang, Effect of calcium ion on phosphate adsorption onto hydrous zirconium oxide, *Chem. Eng. J.*, 2017, **309**, 118–129.

5 IHSS, Acidic Functional Groups of IHSS Samples, http://humic-substances.org/acidic-functional-groups-of-ihss-samples/, (accessed 12 February 2020).

6 T. Ratpukdi, J. A. Rice, G. Chilom, A. Bezbaruah and E. Khan, Rapid Fractionation of Natural Organic Matter in Water Using a Novel Solid-Phase Extraction Technique, *Water Environ. Res.*, 2009, **81**, 2299–2308.

7 H. Walch, A. Praetorius, F. von der Kammer and T. Hofmann, Generation of reproducible model freshwater particulate matter analogues to study the interaction with particulate contaminants, *Water Res.*, 2023, **229**, 119385.

8 H. E. Pace, N. J. Rogers, C. Jarolimek, V. A. Coleman, C. P. Higgins and J. F. Ranville, Determining Transport Efficiency for the Purpose of Counting and Sizing Nanoparticles via Single Particle Inductively Coupled Plasma Mass Spectrometry, *Anal. Chem.*, 2011, **83**, 9361–9369.

9 M. Zlokarnik, in *Ullmann's Encyclopedia of Industrial Chemistry Vol.34*, ed. Wiley-VCH, Wiley, Weinheim, 6th edn., 2012, pp. 433–471.

10 F. Maggi, Variable fractal dimension: A major control for floc structure and flocculation kinematics of suspended cohesive sediment, *J. Geophys. Res.*, 2007, **112**, C07012.

11 M. Elimelech, J. Gregory, X. Jia and R. A. Williams, in *Particle Deposition & Aggregation*, Elsevier, Woburn, 1995, pp. 157–202.

12 J. Gregory, *Particles in Water*, CRC Press, Boca Raton, 2005.

13 H. Wigger, R. Kägi, M. Wiesner and B. Nowack, Exposure and Possible Risks of Engineered Nanomaterials in the Environment—Current Knowledge and Directions for the Future, *Rev. Geophys.*, 2020, **58**, 1–25.

14 F. Gottschalk, T. Sun and B. Nowack, Environmental concentrations of engineered nanomaterials: Review of modeling and analytical studies, *Environ. Pollut.*, 2013, **181**, 287–300.

15 V. Ittekkot, Global trends in the nature of organic matter in river suspensions, *Nature*, 1988, **332**, 436–438.

16 H. Walch, F. von der Kammer and T. Hofmann, Freshwater suspended particulate matter—Key components and processes in floc formation and dynamics, *Water Res.*, 2022, **220**, 118655.